Journal of Materials Chemistry A

PAPER

View Article Online
View Journal | View Issue

Cite this: J. Mater. Chem. A, 2017, 5, 9604

Enhanced storage of sodium ions in Prussian blue cathode material through nickel doping†

Haoyu Fu,[ab] Chaofeng Liu,[abc] Changkun Zhang,[ab] Wenda Ma,[ab] Kan Wang,[ab] Zhuoyu Li,[ab] Xianmao Lu *[ab] and Guozhong Cao *[abc]

Received 5th January 2017
Accepted 18th April 2017

DOI: 10.1039/c7ta00132k

rsc.li/materials-a

Prussian blue (PB) is a promising and cost-effective material for sodium ion batteries (SIBs) because it possesses fast diffusion channels for migration of Na ions and features a two-electron redox reaction mechanism that offers a high theoretical capacity of 170 mA h g^{-1}. However, it is difficult to attain the full discharge capacity of PB in SIBs using the low-spin Fe^{2+}/Fe^{3+} redox couple. In the present study, we found that doping PB with Ni ions (1–10%) resulted in enhanced electrochemical storage capacity and facilitated fast diffusion of Na ions during discharge. Specifically, PB doped with 3% Ni ions showed a discharge capacity of 117 mA h g^{-1}, within which ≈50 mA h g^{-1} was attributed to the low-spin $Fe^{2+}C_6/Fe^{3+}C_6$ redox couple. Even though we do not know how to attain the full storage capacity of PB, this research sheds light on how substituting transition metal ions affects the electrochemical performance of PB. A new perspective of the electrochemical mechanism is also proposed for further understanding and improvement of its electrochemical performance.

Introduction

With the exhaustion of traditional energy resources, an increasing amount of revolutionary renewable energy has been woven into the web of power generation around the world. To facilitate large-scale storage, transportation and application of renewable energy, electrical energy storage (EES) devices are indispensable components.[1–6] Rechargeable batteries have been the most promising choice so far, but recently sodium ion batteries (SIBs) have been growing in popularity because of their reliability.[7–9] Due to the cost-effectiveness and natural abundance of sodium, SIBs have been viewed as competitive candidates for energy storage and conversion.[10–13]

Research into sodium ion energy storage dates back to the 1960s, but SIBs were soon outmatched because they required heating to be fully operational.[14–18] Most recently, extensive studies have been conducted to unveil the potential of an intercalation type of SIB cathode materials such as layered oxides[19–22] and polyanion framework structures,[23–25] although certain intrinsic limitations of these materials need to be solved. Prussian blue and its analogs (PBAs) $A_xM'_y[M''(CN)_6]_z \cdot nH_2O$ (where A is an alkaline metal ion or alkaline earth metal ion, and M′ and M″ are transition metal ions) as a class of low-cost and environment-friendly metal–organic-frameworks (MOFs) emerged as cathode materials for aqueous SIBs in 2011[26] and their performance in non-aqueous SIBs was tested in the following year.[27,28] In typical PB crystal lattices, $M'N_6$ octahedra and $M''C_6$ octahedra are bridged together by cyanide bonds to form a cubic open-framework.[29,30] This loose framework is expected to provide fast diffusion channels for migration of Na ions and suffer little strain during intercalation–deintercalation, attaining good capacity retention at high charge–discharge rates as well as excellent cycling stability.

Despite the high theoretical capacity of PBAs with a two-electron redox reaction,[31] the relatively low capacity contributed by C-coordinated Fe ions and structural instability at high charge/discharge rate are still problematic.[32–34] It is widely acknowledged that $[Fe(CN)_6]^{x-}$ vacancies introduced by the rapid precipitation rate of PBAs and the coordinated water molecules induced by these defects are the main cause of the poor performance of the material.[31,33,35–40] Hence, reducing the defects by slow release of transition metal ions has become a popular approach to synthesize high-quality PB cathode material.[31] This method has been optimized and the as-prepared PB achieved storage capacity performance of 160 mA h g^{-1}.[41] In addition, it has been discovered that heat treatment of graphene-covered PB can also reduce the content of coordinated water.[42]

Substitution of an N-coordinated Fe ion with other transition metal ions is considered to be another effective way to improve the electrochemical performances of electrode materials.[31,37,40,43–47] However, the fast decline of high rate capacity of PBAs is still a challenging issue. Substituting a high-spin Fe ion

[a]Beijing Institute of Nanoenergy and Nanosystems, Chinese Academy of Sciences, Beijing, 100083, China

[b]National Center for Nanoscience and Technology (NCNST), Beijing, 100083, China

[c]Department of Materials Science and Engineering, University of Washington, Seattle, WA 98195-2120, USA. E-mail: gzcao@u.washington.edu

† Electronic supplementary information (ESI) available: TG/DTA curves, XRD patterns, galvanostatic charge/discharge curves at different current densities, EIS and calculated Na ion diffusion coefficient at different discharge states. See DOI: 10.1039/c7ta00132k

with a Ni ion has been reported to improve the cycling stability and rate performance of PBAs, although this was achieved at the expense of storage capacity[44] because Ni ions are inactive within the potential window. Recently, however, it was reported that, apart from these effects, Ni substitution could also enhance the electrochemical activity of C-coordinated Fe ions,[37] but the cause of this phenomenon has yet to be revealed.

We report the effects of Ni doping on the electrochemical performance of PB cathode material. Ni doping was found to activate C-coordinated Fe ions and facilitate fast diffusion of Na ions within the lattice. A capacity of 117 mA h g^{-1} with much improved contribution from low-spin Fe up to 50 mA h g^{-1} was obtained with 3% doping. Doping of Ni ions was also found to slightly promote the stability of the PB lattice even at high charging/discharging rate.

Experimental

Material synthesis

Ni-doped PB was synthesized through a room-temperature co-precipitation method. Specifically, 3 mmol of $Na_4Fe(CN)_6$ was dissolved in 150 mL of distilled water. Then, a 150 mL of mixture solution dissolved with various amounts of $Fe(NO_3)_3$ (3, 2.97, 2.91, 2.85, 2.7 mmol) and $Ni(CH_3COO)_2$ (0, 0.03, 0.09, 0.15, 0.3 mmol) was added dropwise into the $Na_4Fe(CN)_6$ solution under vigorous magnetic stirring. The mixed solution was stirred for an additional 6 h after complete addition and the as-prepared material was collected by centrifugation and washed with distilled water and ethanol several times before being dried under vacuum at 80 °C for 12 h. The samples were denoted as PBA-0, PBA-1, PBA-3, PBA-5 and PBA-10, respectively, according to amount of Ni ions added into the synthesizing solution.

To further confirm the doping effect of the Ni ion, NiFe–PBA was synthesized through a co-precipitation method similar to a process described previously. Specifically, 3 mmol of $Na_4Fe(CN)_6$ was dissolved in 150 mL of distilled water and 3 mmol of $Ni(CH_3COO)_2$ was dissolved in 150 mL of distilled water. Both solutions were mixed and stirred for 6 h. After centrifugation and drying under vacuum 80 °C for 12 h, the as-prepared NiFe–PBA was mixed with PBA-0 at a molar ratio of 3% for an electrochemical test to compare with the performance of PBA-3.

Material characterization

The crystalline structure of the as-prepared material was identified using an X′ Pert 3 diffractometer (PANalytical, the Netherlands) with a Cu Kα radiation source ($\lambda = 1.54056$ Å) and the crystalline size was calculated according to Debye–Scherer formula. Thermogravimetric (Tg) analyses of the samples were conducted on a Mettler Toledo TGA/DSC 1 STAR^e system in flowing Ar at 80–350 °C at a scan rate of 10 °C min^{-1}. The morphology and nanostructure of the samples were examined using field emission scanning electron microscopy (FESEM) using a Nova NanoSEM 450 (FEI) system and field emission transition electron microscopy (FETEM) using a G2 F20 S-TWIN TMP (FEI Tecnai) setup. The elemental analysis of the as-prepared material was performed by energy-dispersive X-ray spectroscopy (EDS). The chemical environment of the C-coordinated Fe ion was examined by Fourier transform infrared (FTIR) spectroscopy with a IRTracer-100 (Shimadzu) with the recording range of the spectra between 300 and 4000 cm^{-1} with a resolution of 4 cm^{-1}.

Electrochemical tests

Electrochemical tests of the samples were conducted in 2032 coin cells. The working electrodes consisted of 70 wt% of the as-prepared material, 20 wt% carbon black, and 10 wt% poly-(vinyldifluoride) (PVDF). The mass loading of the electrodes was 1.32–2.7 mg cm^{-2}. The electrolyte was a 1 M $NaPF_6$ in the mixture of ethylene carbonate (EC) and diethyl carbonate (DEC) (1 : 1 v/v) with 5 wt% fluoroethylene carbonate (FEC) to enhance its cyclic performance. A glass fiber (VWR International) was used as the separator to insulate the working electrode material and sodium metal as the counter electrode. The capacities of the electrode materials were calculated based on the mass of the active material.

Electrochemical tests were conducted at room temperature. Galvanostatic tests were performed on a CT2001A (LAND) system at various current densities. The voltage windows were 2.3–4.0 V (*vs.* Na^+/Na) for capacity retention tests and 2.0–4.0 V (*vs.* Na^+/Na) for cyclic stability tests. Cyclic voltammetry (CV) tests were conducted at a scan rate of 0.1 mV s^{-1} in a potential window of 2.0–4.0 V (*vs.* Na^+/Na) using a SI 1287 electrochemical station (Solartron). The cyclic stabilities of the materials were tested at a current density of 200 mA g^{-1} for 90 cycles after activation at 10 mA g^{-1}. The half-cell EIS tests were conducted before and after the cycling tests using the SI 1287 electrochemical station (Solartron) in conjunction with a 1260 A impedance analyzer (Solartron) over a frequency range from 100 kHz to 0.01 Hz with an AC amplitude of 10 mV.

Results and discussion

The X-ray diffraction (XRD) patterns of all samples could be indexed to be face-centered cubic (JCPDS no. 73-0687) with no detectable parasitic or impurity phase. The diffraction peaks showed relatively low intensities with large full width at half maximum (FWHM) and the average size of PB crystallites was calculated (according to the diffraction peaks of the (200) plane) to be around 12–13 nm regardless of different amounts of Ni doping. Fig. 1a indicates that the diffraction peaks shifted to higher angles after doping of the Ni ion, suggesting contraction of the lattice after the substitution. The lattice-parameter profiles of PBA-0, PBA-1, PBA-3, PBA-5 and PBA-10 were calculated using the program Fullprof (Fig. 1b–f) and the results are summarized in Table 1. The PBA lattice parameter decreased from 10.1816(5) Å for PBA-0 to 10.1740(4) Å for PBA-1, 10.1551(3) Å for PBA-3, 10.1693(4) Å for PBA-5 and 10.1516(3) Å for PBA-10. This result was unexpected because the diameter of the Ni ion is larger than that of the Fe ion, so substitution of the Fe ion by the Ni ion usually leads to lattice expansion.[39,46] By calculation according to the lattice parameter of various

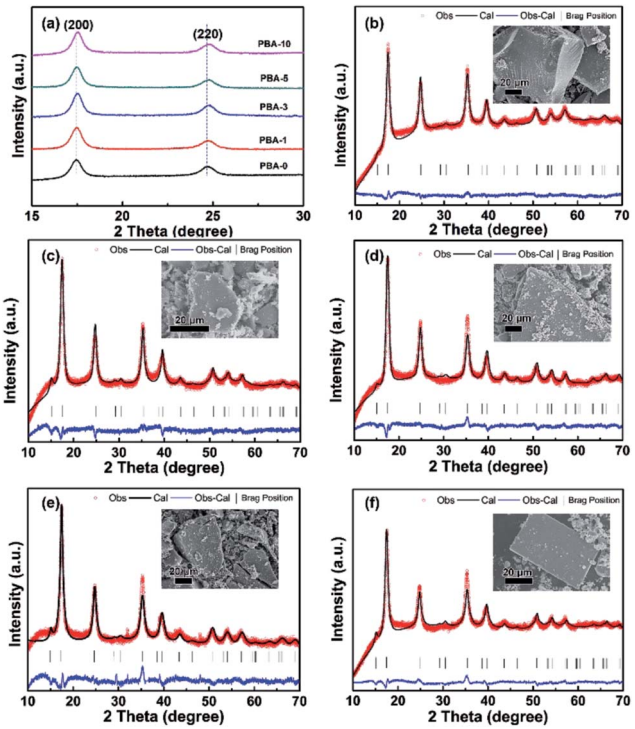

Fig. 1 The lattice parameters of pristine PB and Ni-doped PB were examined *via* XRD and refined according to the Rietveld method. (a) The XRD peaks of all samples with 2θ in the range of 15–30° were obtained. The XRD peaks of Ni-doped samples shifted to a higher angle, indicating contraction of the material. Rietveld refinements of XRD patterns of (b) PBA-0, (c) PBA-1, (d) PBA-3, (e) PBA-5, and (f) PBA-10. The insets of (b)–(f) are SEM images of the corresponding samples.

Table 1 Lattice parameters of the as-prepared PB samples characterized by XRD and contents of coordinated water molecules determined by TGA

	A (Å)	R_p (%)	R_{wp} (%)	χ^2	Coordinated water
PBA-0	10.1816(5)	1.24	1.61	4.07	10.5%
PBA-1	10.1740(4)	1.29	1.69	4.74	10.2%
PBA-3	10.1551(3)	1.47	2.05	6.80	14.6%
PBA-5	10.1693(4)	1.42	1.98	5.86	15.9%
PBA-10	10.1516(3)	1.56	2.12	6.80	16.1%

transition metal ion (Fe^{3+}, Cu^{2+}, Ni^{2+}, Co^{2+}) ferrocyanides and Goldschmidt ionic radii of these transition metal ions, Brown *et al.* claimed that the ionic radius of ferrocyanide decreased from 4.55 Å in $Fe^{III}Fe^{II}$–PBA to 4.32 Å in $Ni^{II}Fe^{II}$–PBA.[48] This result suggests that a small amount of substitution of Ni^{2+} could lead to reduced lattice constants in the PB lattice. Conversely, the relatively large lattice parameter of sample PBA-5 could be attributed to the changed content in zeolite water molecules because sample PBA-5 was likely to lose more zeolite water molecules during drying and result in lattice expansion.[49,50] Nonetheless, all doped samples showed lattice contraction.

In addition, substitution of N-coordinated Fe^{3+} with Ni^{2+} would introduce $[Fe(CN)_6]^{x-}$ vacancies to maintain the electroneutrality of the lattice. Therefore, a higher content of Ni^{2+} corresponded to more coordinated water. A TG test was applied to determine the coordinated water content of the lattices (Fig. S1a–e†). The weight loss <200 °C was related to the loss of absorbed water and zeolite water, and the weight loss between 200 °C and 250 °C corresponded to the loss of coordinated water. The differential thermal analysis (DTA) peak at 225 °C indicated breakage of the Fe–O bond, namely, the breakage of coordinated water from the lattice.[44,50] After dehydration of the lattice >250 °C, the material decomposed slowly by reacting with water molecules and finally producing Fe_2O_3 (JCPDS no. 73-0603 and no. 86-0550), which was confirmed by XRD patterns (Fig. S1f†). TG results are summarized in Table 1 and indicate introduction of $[Fe(CN)_6]^{x-}$ vacancies by an increased Ni ion doping amount, confirming the success of doping.

The morphology of the as-prepared material was characterized by SEM (insets in Fig. 1). All products were micron-scale aggregated particles. There was no obvious difference in morphology among the samples, so the doping of the Ni ion had little influence on the formation of the PB material. TEM characterization in Fig. 2 demonstrates more details of the aggregates. As shown in Fig. 2a, the aggregates consisted of many nanoparticles and the selected area electron diffraction (SAED) image in Fig. 2a could be indexed to the (200), (220), (400), (420) and (422) lattice planes of PB. Observation of the nanoparticles on the aggregates (Fig. 2b) confirmed that the sizes of the nanoparticles were around 7–15 nm, consistent with the particle size calculated from XRD peaks using the Scherrer equation.[51] The observed lattice plane in Fig. 2b could be indexed to (400) and (420) of PB, consistent with the SAED

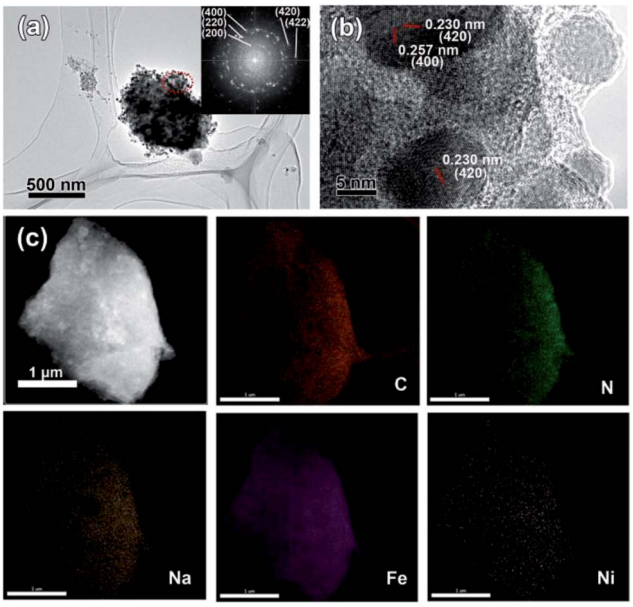

Fig. 2 (a) TEM image of PBA-3; the inset of (a) is the corresponding SAED. (b) TEM image showing particles within aggregates. These results indicate that the aggregates consisted of nanoparticles with sizes of 7–15 nm. (c) EDS mapping of PBA-3 showing uniform distribution of C, N, Na, Fe, and Ni.

image. In addition, the nanoparticles on the aggregates seemed to be covered with an amorphous layer. PB-type materials are sensitive to electron beams, so this observed layer could be attributed to the interaction between the material and electron beam.[33] EDS mapping of the aggregates (Fig. 2c and S2†) further confirmed uniform distribution of Fe and Ni in the material. EDS elemental analyses (Fig. S3†) of all samples showed gradually increased Ni content from PBA-1 to PBA-10.

FTIR spectroscopy was applied to probe the doping effect on the Fe–C bond and –C≡N– bond. As shown in Fig. 3a, the band in the region 450–650 cm^{-1} corresponded to the bending mode of Fe–C≡N–M (M = Fe or Ni), whereas the 600 cm^{-1} band was associated with a Fe–C≡N vibration mode.[49] No obvious broad band was shown between 350 and 450 cm^{-1}, indicating that the as-prepared PB was soluble, consistent with what was observed during the synthesis. Details of FTIR spectra between 350 and 650 cm^{-1} are shown in Fig. 3b. The electronegativity of Ni^{2+} (1.91) is lower than that of the substituted Fe^{3+} (1.96), so the substitution would induce an inductive effect that would cause the shift of the electron cloud on the Fe–C bond towards the CN ligand, causing a red-shifted band at 600 cm^{-1}.[52] The shift of the electron cloud is equivalent to raising C-coordinated Fe ions to a more positive valence state, thereby enhancing their electrochemical activity.[47] This observed phenomenon could be closely related to the dopant's influence on the electron atmosphere of the low-spin Fe ion reported previously.[37] Although there was a subtle red shift (≈1 cm^{-1}) at 600 cm^{-1}, it was not conclusive because the test resolution was 4 cm^{-1}. The band at ≈2080 cm^{-1} corresponded to the stretching vibration of the –C≡N– bond, further confirming the formation of PB.[53,54] The weak band at 1611 cm^{-1} and broad band at 3449 cm^{-1} could be attributed to the water molecules in the lattice. The vibration band between 1385 and 1400 cm^{-1} could be related to the nitrates used in the synthesis.[53]

The electrochemical performances of all samples were tested first *via* galvanostatic and CV methods. As shown in the charge/discharge profiles at a current density of 10 mA g^{-1} (Fig. 4a), PBA-1, PBA-3, PBA-5 clearly showed improved storage capacities with the largest discharge capacity of 117 mA h g^{-1} being delivered by PBA-3. However, PBA-10 showed a diminished capacity caused by a decreased capacity contribution of the discharge plateau of high-spin transition metal ions. The loss of capacity could be attributed to a higher percentage of electrochemically inactive N-coordinated Ni ions and inhibited

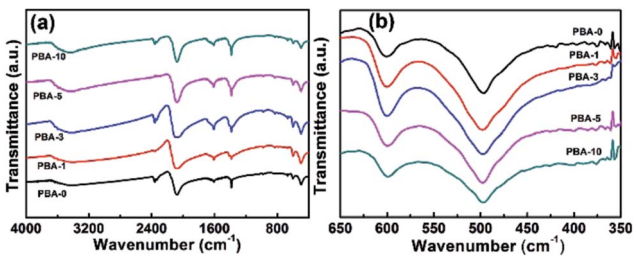

Fig. 3 (a) FTIR spectra of PBA-0, PBA-1, PBA-3, PBA-5 and PBA-10. (b) FTIR spectra of all samples at wave numbers between 350 and 650 cm^{-1}.

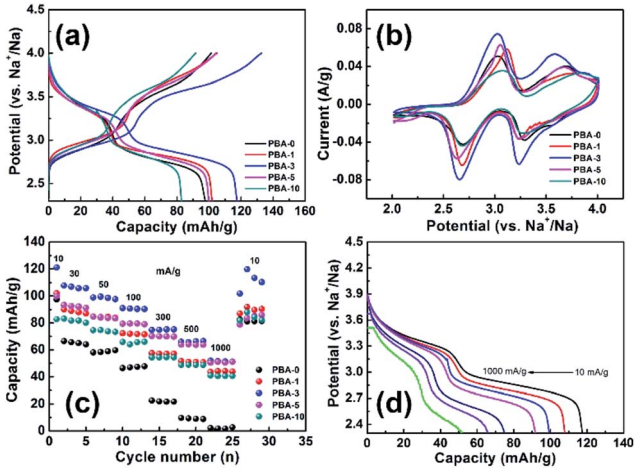

Fig. 4 (a) Galvanostatic curves of all samples at a current density of 10 mA g^{-1}; (b) cyclic voltammetry curves at a scan rate of 0.1 mV s^{-1}; (c) rate performances of PBA samples at current densities ranging from 10 to 1000 mA g^{-1}; (d) galvanostatic discharge curves of PBA-3 at various current densities.

diffusion of Na ions induced by coordinated water molecules. Further examination of the discharge profiles revealed that the capacity contribution of low-spin Fe ions increased up to 50 mA h g^{-1} with doping of the Ni ion (Fig. S4†), which is a dramatic improvement for the low-spin Fe^{2+}/Fe^{3+} redox couple. Similar results have been reported.[37] This improved electrochemical performance of doped PB at a higher potential could be attributed to the weaker crystal field splitting experienced by the C-coordinated Fe ion after doping of Ni, which makes it easier for electrons to transfer from the e_g to t_{2g} orbitals of Fe^{3+} during discharge.[47]

To further confirm successful doping of the Ni ion, pristine PBA-0 was mixed with a 3% molar ratio of NiFe–PBA. The mixed powder was tested by galvanostatic methods and compared with PBA-3. As shown in Fig. S5,† the mixed powder yielded a capacity of only 25 mA h g^{-1} from a C-coordinated Fe^{2+}/Fe^{3+} redox couple. This comparison indicated that the promoted performance could be attributed to a Ni-doped phase.

The CV curves of all samples are shown in Fig. 4b. In general, the charge/discharge of the material showed a two-step process. The peaks of the redox couples are summarized in Table 2. The half-wave potentials of all samples were 3.5 V (*vs.* Na/Na^+) for the $Fe^{2+}C_6/Fe^{3+}C_6$ redox couple and 2.85 V (*vs.* Na/Na^+) for the $Fe^{2+}N_6/Fe^{3+}N_6$ redox couple, which were consistent with

Table 2 Cyclic voltammetry peaks of PB samples (numbers within the brackets correspond to the potential intervals of the redox peaks)

	High spin redox couple	Low spin redox couple
PBA-0	3.02/2.69(0.33)	3.69/3.28(0.41)
PBA-1	3.12/2.68(0.44)	3.74/3.23(0.51)
PBA-3	3.02/2.65(0.37)	3.58/3.23(0.36)
PBA-5	3.05/2.63(0.42)	3.67/3.23(0.44)
PBA-10	3.07/2.68(0.39)	3.82/3.26(0.56)

galvanostatic tests. The redox potential for the high-spin Fe ion deviating from 3.0 V (*vs.* Na/Na^+) to a lowered potential could be attributed to the charge-spin lattice coupling effect associated with lattice distortion.[38] These results demonstrated the improved electrochemical reversibility of the redox couples of PBA-3, especially for the redox couple related to a low-spin Fe ion. Conversely, the higher peak intervals of PBA-5 and PBA-10 indicated lowered electrochemical reversibility induced by a larger amount of coordinated water. Moreover, the peak intervals for PBA-1 were unusually high and their electrochemical behavior will be studied by electrochemical impedance spectrometry (EIS).

The capacity retentions of all samples were tested at different current densities (10 mA g^{-1} to 1000 mA g^{-1}) (Fig. 4c). The capacity of pristine PBA-0 dropped dramatically with an increased charge/discharge rate (Fig. S6a†), whereas the other four samples retained 40–60 mA h g^{-1} at 1000 mA g^{-1}, indicating an improved high rate performance of Ni-doped PB. On careful examination of the discharge curves of PBA-3 (Fig. 4d), it was found that the high rate capacity of the Ni-doped PB cathode material was mostly contributed by a low-spin $Fe^{2+}C_6$/$Fe^{3+}C_6$ redox couple. This system was identical to other Ni-doped PB samples (Fig. S6b–d†). It has been reported that the sodiation process associated with the C-coordinated Fe^{2+}/Fe^{3+} redox reaction has little impact on structure. As the sodiation process proceeds, the intercalation/deintercalation of Na ions would introduce cubic-rhombohedral phase transition at a lower discharge plateau. Hence, the phase separation would induce irreversibility at a higher charge/discharge rate, causing a reduced capacity contribution of the high-spin Fe ion.[40,47] Also, when obtaining electrons, a high-spin Fe^{3+} would introduce a higher cost of on-site electron–electron coulomb energy and resulted in inhibition of the reaction rate of the high-spin $Fe^{2+}N_6/Fe^{3+}N_6$ redox couple.[41] Therefore, it can be concluded that the high rate performance of Ni-doped PB cathode material was mainly contributed by the capacity of the low-spin $Fe^{2+}C_6$/$Fe^{3+}C_6$ redox couple. Activating the C-coordinated Fe ion by doping the Ni ion can improve the capacity retention and energy density of the material.

The cycling stability of the samples was tested at a current density of 200 mA g^{-1} for 90 cycles (Fig. 5a). The capacity retentions were 82.8% for PBA-0, 83% for PBA-1, 86.3% for PBA-3, 88.3% for PBA-5 and 90.8% for PBA-10. The cycling performance of PB was improved with doping amount. This result was expected because the electrochemically inactive Ni ion could stabilize the lattice during the repeating sodiation/desodiation process.[37,55] The galvanostatic curves of PBA-3 during the cycling test are shown in Fig. 5b, and the result suggests that the capacity loss during the cycling test could mainly be attributed to the capacity fading at the high-spin Fe^{2+}/Fe^{3+} redox couple. The faded discharge capacity contribution of the $Fe^{2+}N_6/Fe^{3+}N_6$ redox couple could be attributed to the irreversibility caused by phase separation, as mentioned above. Moreover, the cycling-tested samples showed an expanded lattice (Fig. S7†), suggesting gradual accumulation of residual Na^+ during the charge/discharge process.

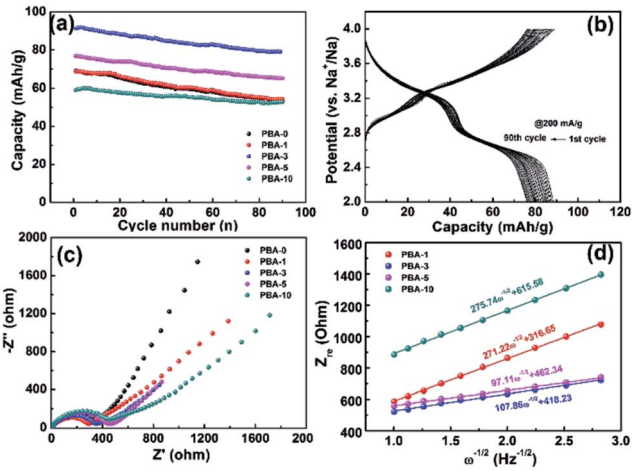

Fig. 5 (a) Cycling stability of all samples tested by galvanostatic methods at 200 mA g^{-1} for 90 cycles; (b) galvanostatic curves of PBA-3 from the 1st cycle to the 90th cycle. This result suggests that the capacity loss during the cycling test of Ni-doped PB material could be mainly attributed to the irreversibility of the high-spin $Fe^{2+}N_6/Fe^{3+}N_6$ redox couple; (c) EIS spectra of PB samples after a cycling test; (d) fittings of Z_{re} *versus* reciprocal square root of the angular frequency at the low-frequency region of Nyquist plots.

EIS is a valuable method to study the kinetics of the transportation of Na ions at the electrode/electrolyte interface and their diffusion within the lattice. All samples were tested before cycling (Fig. S8a†), and the electrolyte impedance R_s of the samples was identified to be ≈10 Ω. The high-frequency regions of the EIS spectra of the samples showed two identical semi-circles. This impedance behavior could be attributed to the adion insertion mechanism of Na^+.[56–58] This mechanism suggested that the charge transfer of Na^+ from the electrolyte to the electrode went through two interfaces: the outer Helmholtz plane (OHP)/inner Helmholtz plane (IHP) interface and IHP/electrode interface. Hence, the impedance behavior of PBA in a high-frequency region can exhibit two semi-circles. However, after one charge/discharge cycle at 10 mA g^{-1} (Fig. S8b†), the impedance of Na^+ charge transfer at the OHP/IHP interface of samples declined quickly, and the charge transfer impedance was mainly attributed to impedance at the interface of the electrolyte and electrode. The reason for this phenomenon could be the easy solvation/desolvation process of Na^+, resulting in fast charge transfer at the OHP/IHP interface. As shown in the inset of Fig. S7b,† the R_{ct} of PBA-3 and PBA-5 was 1250 Ω and 885 Ω, respectively, whereas the R_{ct} of PBA-0 was 2328 Ω. However, the high-frequency region of EIS spectra of PBA-1 and PBA-10 suggested the persistence of OHP/IHP impedance, the reason for which is not known. Consecutively, after 10 cycles at a current density of 200 mA g^{-1} (Fig. S8c†), the R_{ct} of PBA-0, PBA-3, PBA-5 and PBA-10 reduced further to 623 Ω, 593 Ω, 537 Ω and 485 Ω, respectively, but the influence of the OHP/IHP interface for PBA-1 persisted even after 10 cycles. However, after 90 cycles at a current density of 200 mA g^{-1}, the EIS spectra of the five samples (Fig. 5c) showed an R_{ct} of 506 Ω for PBA-0, 319 Ω for PBA-1, 380 Ω for PBA-3, 453 Ω for PBA-5 and 491 Ω

for PBA-10. The lowered charge transfer impedance of all samples after cycle tests could be the result of a PB-type material losing zeolite water molecules during the charge process.[28,38] The R_{ct} of the samples was small for the PBA electrode material, so it could deliver excellent electrochemical performance.[44,46]

The linear part of the EIS spectra at low frequencies is associated with diffusion of Na ions within the material. The Na-ion diffusion coefficient D of Ni-doped PB can be calculated according to the following equation:

$$D = R^2T^2/2A^2n^4F^4C^2\sigma^2 \quad (1)$$

where R is the gas constant, T is the absolute temperature, A is the surface area of the electrode, n is the number of electrons transferred per molecule during the redox reaction, F is the Faraday constant, C is the concentration of the Na ion within the electrolyte (1.3×10^{-3} mol cm^{-3}) and σ is the Warburg factor.[44] According to eqn (1), the Na-ion diffusion coefficient of PBA-1, PBA-3, PBA-5 and PBA-10 was calculated to be 7.18×10^{-14} cm^2 s^{-1}, 4.54×10^{-13} cm^2 s^{-1}, 5.60×10^{-13} cm^2 s^{-1} and 6.94×10^{-14} cm^2 s^{-1}, respectively. Substitution of the Ni ion has been reported to facilitate faster diffusion of the Na ion within PBA lattices,[44] which allows for improved performance of the C-coordinated Fe^{3+}/Fe^{2+} redox couple. However, if the doping amount was increased to 10%, the introduced defects would greatly limit the diffusion rate of Na ions, resulting in a lowered diffusion coefficient for Na ions.

Conclusions

A small amount of Ni ion doping in PB cathode material was found to substitute for high-spin Fe ions and improve the sodium ion storage capacity of a low-spin Fe^{2+}/Fe^{3+} redox couple up to 50 mA h g^{-1}. The doping of Ni ions lowered the bond force constant of Fe–C≡N, leading to electrochemical activation of C-coordinated Fe ions. In addition, substitution with Ni ions could facilitate a higher diffusion rate of Na ions and stabilize the PB lattice, resulting in an improved rate and cyclic performance. The best electrochemical performance was attained with 3% Ni doping, whereas higher doping content of electrochemically inactive Ni led to lowered storage capacity.

Acknowledgements

This work was supported by the Thousand Talents Program for Pioneer Researchers and its Innovation Team, China.

Notes and references

1 M. Armand and J. M. Tarascon, *Nature*, 2008, **451**, 652–657.
2 B. Dunn, H. Kamath and J. M. Tarascon, *Science*, 2011, **334**, 928–935.
3 J. B. Goodenough, *Energy Storage Materials*, 2015, **1**, 158–161.
4 Q. Zhang, E. Uchaker, S. L. Candelaria and G. Cao, *Chem. Soc. Rev.*, 2013, **42**, 3127–3171.
5 R. C. Massé, E. Uchaker and G. Cao, *Sci. China Mater.*, 2015, **58**, 715–766.
6 C. Liu, Z. G. Neale and G. Cao, *Mater. Today*, 2016, **19**, 109–123.
7 H. Kim, H. Kim, Z. Ding, M. H. Lee, K. Lim, G. Yoon and K. Kang, *Adv. Energy Mater.*, 2016, **6**, 1600943.
8 E. Uchaker, Y. Z. Zheng, S. Li, S. L. Candelaria, S. Hu and G. Z. Cao, *J. Mater. Chem. A*, 2014, **2**, 18208–18214.
9 Q. Zhou, L. Liu, Z. Huang, L. Yi, X. Wang and G. Cao, *J. Mater. Chem. A*, 2016, **4**, 5505–5516.
10 M. D. Slater, D. Kim, E. Lee and C. S. Johnson, *Adv. Funct. Mater.*, 2013, **23**, 947–958.
11 H. Pan, Y.-S. Hu and L. Chen, *Energy Environ. Sci.*, 2013, **6**, 2338–2360.
12 V. Palomares, M. Casas-Cabanas, E. Castillo-Martinez, M. H. Han and T. Rojo, *Energy Environ. Sci.*, 2013, **6**, 2312–2337.
13 D. Kundu, E. Talaie, V. Duffort and L. F. Nazar, *Angew. Chem., Int. Ed.*, 2015, **54**, 3431–3448.
14 Y.-F. Y. Yao and J. T. Kummer, *J. Inorg. Nucl. Chem.*, 1967, **29**, 2453–2459.
15 J. B. Goodenough, H. Y.-P. Hong and J. A. Kafalas, *Mater. Res. Bull.*, 1976, **11**, 203–220.
16 M. S. Whittingham, *J. Solid State Chem.*, 1978, **12**, 41–99.
17 A. S. Nagelberg and W. L. Worrell, *J. Solid State Chem.*, 1979, **29**, 345–354.
18 A. Van Zyl, *Solid State Ionics*, 1996, **86**, 883–889.
19 I. Hasa, D. Buchholz, S. Passerini and J. Hassoun, *ACS Appl. Mater. Interfaces*, 2015, **7**, 5206–5212.
20 D. Buchholz, C. Vaalma, L. G. Chagas and S. Passerini, *J. Power Sources*, 2015, **282**, 581–585.
21 J. L. Yue, W. W. Yin, M. H. Cao, S. Zulipiya, Y. N. Zhou and Z. W. Fu, *Chem. Commun.*, 2015, **51**, 15712–15715.
22 G. Singh, F. Aguesse, O. Laida, E. Goikolea, E. Gonzalo, J. Segalini and T. Rojo, *J. Power Sources*, 2015, **273**, 333–339.
23 Z. Jian, L. Zhao, H. Pan, Y.-S. Hu, H. Li, W. Chen and L. Chen, *Electrochem. Commun.*, 2012, **14**, 86–89.
24 Z. Chu and C. Yue, *Solid State Ionics*, 2016, **287**, 36–41.
25 D. Kundu, R. Tripathi, G. Popov, W. R. M. Makahnouk and L. F. Nazar, *Chem. Mater.*, 2015, **27**, 885–891.
26 C. D. Wessells, S. Pedadda, R. A. Huggins and Y. Cui, *Nano Lett.*, 2011, **11**, 5421–5425.
27 H. Lee, Y.-I. Kim, J. K. Park and J. W. Choi, *Chem. Commun.*, 2012, **48**, 8416–8418.
28 Y. Lu, L. Wang, J. Cheng and J. B. Goodenough, *Chem. Commun.*, 2012, **48**, 6544–6546.
29 A. Ludi, *Inorg. Chem.*, 1980, **19**, 956.
30 A. Ludi and H. U. Güdel, *Structrual Chemistry of Polynuclear Transition Metal Cyanides*, 1970.
31 Y. You, X.-L. Wu, Y.-X. Yin and Y.-G. Guo, *Energy Environ. Sci.*, 2014, **7**, 1643–1647.
32 X. Wu, W. Deng, J. Qian, Y. Cao, X. Ai and H. Yang, *J. Mater. Chem.*, 2013, **1**, 10130–10134.
33 W.-J. Li, S.-L. Chou, J.-Z. Wang, Y.-M. Kang, J.-L. Wang, Y. Liu, Q.-F. Gu, H.-K. Liu and S.-X. Dou, *Chem. Mater.*, 2015, **27**, 1997–2003.
34 Q. Meng, W. Zhang, M. Hu and J.-S. Jiang, *Chem. Commun.*, 2016, **52**, 1957–1960.

35 X. Wu, Y. Luo, M. Sun, J. Qian, Y. Cao, X. Ai and H. Yang, *Nano Energy*, 2015, **13**, 117–123.
36 Y. Liu, Y. Qiao, W. Zhang, Z. Li, X. Ji, L. Miao, L. Yuan, X. Hu and Y. Huang, *Nano Energy*, 2015, **12**, 386–393.
37 S. Yu, Y. Li, Y. Lu, B. Xu, Q. Wang, M. Yan and Y. Jiang, *J. Power Sources*, 2015, **275**, 45–49.
38 J. Song, L. Wang, Y. Lu, J. Liu, B. Guo, P. Xiao, J.-J. Lee, X.-Q. Yang, G. Henkelman and J. B. Goodenough, *J. Am. Chem. Soc.*, 2015, **137**, 2658–2664.
39 D. Yang, J. Xu, X.-Z. Liao, Y.-S. He, H. Liu and Z.-F. Ma, *Chem. Commun.*, 2014, **50**, 13377–13380.
40 X. Wu, C. Wu, C. Wei, L. Hu, J. Qian, Y. Cao, X. Ai, J. Wang and H. Yang, *ACS Appl. Mater. Interfaces*, 2016, **8**, 5393–5399.
41 L. Wang, J. Song, R. Qiao, L. A. Wray, M. A. Hossain, Y.-D. Chuang, W. Yang, Y. Lu, D. Evans, J.-J. Lee, S. Vail, X. Zhao, M. Nishijima, S. Kakimoto and J. B. Goodenough, *J. Am. Chem. Soc.*, 2015, **137**, 2548–2554.
42 D. Yang, J. Xu, X.-Z. Liao, H. Wang, Y.-S. He and Z.-F. Ma, *Chem. Commun.*, 2015, **51**, 8181–8184.
43 T. Matsuda, M. Takachi and Y. Moritomo, *Chem. Commun.*, 2013, **49**, 2750–2752.
44 Y. You, X.-L. Wu, Y.-X. Yin and Y.-G. Guo, *J. Mater. Chem. A*, 2013, **1**, 14061–14065.
45 H.-W. Lee, R.-Y. Wang, M. Pasta, S. W. Lee, N. Liu and Y. Cui, *Nat. Commun.*, 2014, **5**, 5280–5285.
46 M. Xie, M. Xu, Y. Huang, R. Chen, X. Zhang, L. Li and F. Wu, *Electrochem. Commun.*, 2015, **59**, 91–94.
47 M. Pasta, R. Y. Wang, R. Ruffo, R. Qiao, H.-W. Lee, B. Shaym, M. Guo, Y. Wang, L. A. Wray, W. Yang, M. F. Toney and Y. Cui, *J. Mater. Chem. A*, 2016, **4**, 4211–4223.
48 D. B. Brown, D. F. Shriver and L. H. Schwartz, *Inorg. Chem.*, 1968, **7**, 77–83.
49 R. E. Wilde, S. N. Ghosh and B. J. Marshall, *Inorg. Chem.*, 1970, **9**, 2512–2516.
50 N. Imanishi, T. Morikawa, J. Kondo, Y. Takeda, O. Yamamoto, N. Kinugasa and T. Yamagishi, *J. Power Sources*, 1999, **79**, 215–219.
51 A. L. Patterson, *Phys. Rev.*, 1939, **56**, 978–982.
52 L. M. Stock, *J. Chem. Educ.*, 1972, **49**, 400.
53 S. Ayrault, B. Jimenez, E. Garnier, M. Fedoroff, D. J. Jones and C. Loos-Neskovic, *J. Solid State Chem.*, 1998, **141**, 475–485.
54 M. J. Piernas-Muñoz, E. Castillo-Martínez, V. Roddatis, M. Armand and T. Rojo, *J. Power Sources*, 2014, **271**, 489–496.
55 D. Asakura, C. H. Li, Y. Mizuno, M. Okubo, H. Zhou and D. R. Talham, *J. Am. Chem. Soc.*, 2013, **135**, 2793–2799.
56 Y. Mizuno, M. Okubo, D. Asakura, T. Saito, E. Hosono, Y. Saito, K. Oh-ishi, T. Kudo and H. Zhou, *Electrochim. Acta*, 2012, **63**, 139–145.
57 P. G. Bruce and M. Y. Saidi, *J. Electroanal. Chem.*, 1992, **322**, 93–105.
58 P. G. Bruce and M. Y. Saidi, *Solid State Ionics*, 1992, **51**, 187.